



Influence of the preparation method and aluminum ion substitution on the structure and electrical properties of lithium–iron ferrites

L. S. Kaykan¹ · A. K. Sijo² · J. S. Mazurenko³ · A. Żywczak⁴

Received: 21 December 2020 / Accepted: 19 January 2021
© King Abdulaziz City for Science and Technology 2021

Abstract

In this study, we report the synthesis of nanosized Al-substituted lithium–iron ferrites $\text{Li}_{0.5}\text{Al}_x\text{Fe}_{2.5-x}\text{O}_4$ ($0 \leq x \leq 1$) by sol–gel auto-combustion method and by ceramic method with double sintering. Synthesized materials were studied using X-ray diffraction and impedance spectroscopy. The samples obtained by chemical methods have a higher homogeneity of the distribution of elements by volume, good repeatability of the result, high crystallinity, small crystallite size and perfect stoichiometry. Based on Koop's theory, the basic regularities of the behavior of the dielectric constant and the loss tangent are explained. The jump mechanism of conductivity has been realized by the transition of an electron between iron ions in different valence states. Samples synthesized by the sol–gel auto-combustion show technological characteristics, compared with systems obtained by solid-phase method.

Keywords Nanoparticles · Sol–gel · Spinel ferrite · X-ray diffraction · Electrical properties · Dielectric constant

Introduction

Ferrites have many applications as electrical materials in a wide frequency range due to their high resistance and relatively low losses (Kopayev et al. 2015). Therefore, studies of the behavior of the dielectric properties of such materials at different frequencies are of considerable interest (Ostafiychuk et al. 2016). The dielectric properties of ferrites depend on a number of factors, such as the method of preparation, processing temperature, sintering conditions,

chemical composition, cationic distribution and crystallite size (Argentina and Baba 1974; Kaykan et al. 2019).

The preparation of ferrites is of particular importance in the formation of their properties, because the size of the ferrite particles determine the properties of the material: whether it is superparamagnetic, single-domain or multi-domain, as well as the conductive and dielectric properties vary greatly depending on the method of preparation (Ostafiychuk et al. (2015)). One of the simplest, most affordable and cheapest ways to synthesize nanosized ferrites with a spinel structure is the sol–gel auto-combustion method. Along with simplicity and availability, this method does not demand high temperatures (Sijo et al. 2020) and long annealing and gives the chance to increase size of nano-particles (Sijo and Dutta 2018).

Lithium and substituted lithium ferrites play an important role in microwave technology and memory cells due to the high Curie temperature, high saturation magnetization, excellent hysteresis loops and low voltage sensitivity (Soman et al. 2013; Sijo et al. 2017). In addition, lithium ferrites do not contain expensive components (Khan et al. 2020). Lithium ferrites behave like an n-type semiconductor with an inverse spinel structure and have a high electrical resistance ($10^5 \Omega$ – $10^6 \Omega$) and high Curie temperature (640 °C–680 °C), and can be used in gas sensors (Manikandan et al. 2018, 2019).

✉ L. S. Kaykan
larysa.kaykan@gmail.com

A. K. Sijo
sijoaracka@gmail.com

¹ G.V. Kurdyumov Institute for Metal Physics, N.A.S. of Ukraine, 36 Academician Vernadsky Boulevard, Kiev 03142, Ukraine

² Department of Physics, Mary Matha Arts and Science College, Mananthavady, Kerala 670645, India

³ Ivano Frankivsk National Medical University, Halytska Str. 2, Ivano-Frankivsk 76018, Ukraine

⁴ Academic Centre for Materials and Nanotechnology, AGH University of Science and Technology, Krakow 30-059, Poland

At low temperatures, the compound manifests itself as an inverse spinel in which Li^+ and $3/5\text{Fe}^{3+}$ occupy the B-position, and the remaining ions Fe^{3+} occupy the A position and form a spatial group $\text{P4}_3\text{32}$. At temperatures above $735\text{ }^\circ\text{C}$ – $755\text{ }^\circ\text{C}$ the population of octahedral B-positions becomes disordered and the spatial group becomes Fd3m (Patil et al. 2012). Synthesis and structural stability of lithium ferrites with and without impurities remain at the peak of research in the field of magnetic materials. Substitution by trivalent cations that provide charge neutrality is one of the important areas of structure modification. Such mixed lithium ferrites are unique because they do not contain any divalent cations.

This paper reports synthesis and analysis of aluminum-substituted ferrites $\text{Li}_{0.5}\text{Al}_x\text{Fe}_{2.5-x}\text{O}_4$ ($0 \leq x \leq 1$), obtained by sol–gel auto-combustion method and by ceramic method with double sintering.

Experimental

Nanoparticles of $\text{Li}_{0.5}\text{Al}_x\text{Fe}_{2.5-x}\text{O}_4$ ($0.0 \leq x \leq 1.0$) were obtained by two methods: traditional solid-state reaction and sol–gel auto-combustion method, for which analytical quantities of LiNO_3 (anhydrous), $\text{Fe}(\text{NO}_3)_3 \cdot 9\text{H}_2\text{O}$ and $\text{Al}(\text{NO}_3)_3 \cdot 9\text{H}_2\text{O}$ were used as starting materials. Metal nitrates were stoichiometrically dissolved in a 20 ml amount of distilled water and mixed dropwise together with constant stirring. To a mixture of metal nitrates, a solution of citric acid in a molar ratio of 1:1.75 was added. The pH of the pure solution was equal to one. To the mixture of solutions, dropwise with constant stirring 30% ammonium solution was added to reach pH value equal to seven. The resulting solution was kept in an oven at $70\text{ }^\circ\text{C}$ until gel formation. Gel formation occurred as a result of the binding of metal-carboxyl complexes into a three-dimensional structure. The formed gel was placed in a muffle oven and heated to a temperature of approximately $250\text{ }^\circ\text{C}$.

To compare the properties and establish the effect of the surface on the physicochemical properties of the material, we synthesized a compound of the same composition by the traditional ceramic method of double sintering. The starting precursors were powders of Al_2O_3 , Fe_2O_3 and Li_2CO_3 (reagent grade, the content of the main component can be higher or significantly higher than 98%), weighed in stoichiometric ratio precursors carefully milled and mixed with a planetary mill for 5 h. After the addition of the binder, balls of the same size were formed, which were subjected to pre-sintering at a temperature of $950\text{ }^\circ\text{C}$ for 5 h. Next, the cooled samples were subjected to re-grinding and homogenization, after which tablets were formed. These tablets were sintered at a temperature of $1200\text{ }^\circ\text{C}$ for 5 h.

Obtained $\text{Li}_{0.5}\text{Al}_x\text{Fe}_{2.5-x}\text{O}_4$ powders were characterized using Rigaku Ultima-IV X-ray diffractometer in $\text{CuK}\alpha$ radiation at temperature 293 K to establish phase purity and crystallinity. The average crystallite size was determined by the Debye–Scherrer formula (Ostafiychuk et al. 2017). The contribution to the half-width due to instrumental broadening was also taken into account using a standard silicon sample when calculating the size of the crystallites. (Ostafiychuk et al. 2017). The X-ray density and porosity of all samples were determined using Archimedes' principle. The capacitance, dielectric constants and impedance were measured in the frequency range 0.01 – 105 Hz using LCR HI-Tester (HIOKI 3532–50) and impedance spectrometer. All samples were made in the form of pellets, which were coated with graphite at both ends to create parallel plates of the capacitor with a ferrite material as a dielectric medium. Studies on the impedance spectrometer were carried out by the powder method. The substance was placed in a fluoroplastic capsule and compressed under low pressure. To calculate frequency dependences of the specific conductivity and resistance, the inner diameter of the capsule and height of the column of the powder sample were recorded.

Results and discussion

X-ray analysis

The X-ray spectra of $\text{Li}_{0.5}\text{Al}_x\text{Fe}_{2.5-x}\text{O}_4$ ($0 \leq x \leq 1$) samples synthesized by sol–gel auto-combustion are shown in

Fig. 1, which indicates single-pure phase cubic spinel structure of the spatial group Fd3m . The average broadening of 311 peak is observed in all spectra indicates nano crystalline nature of particles. The crystallite sizes of the samples

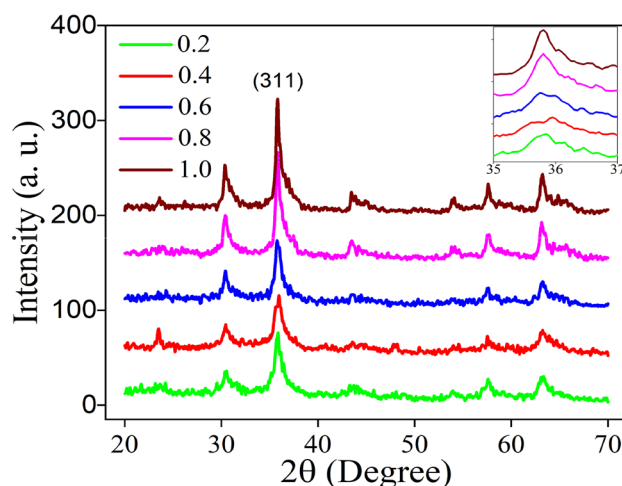
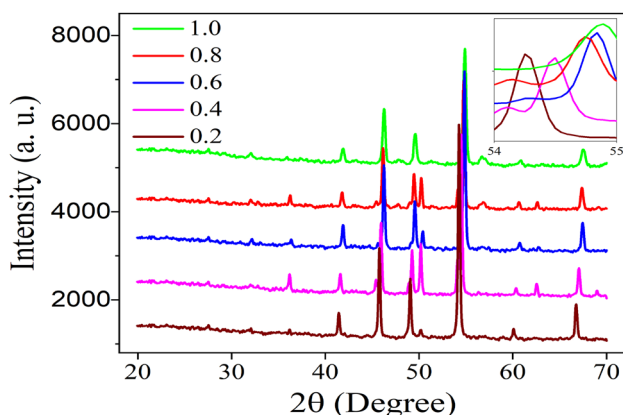


Fig. 1 X-ray diffraction spectra of $\text{Li}_{0.5}\text{Al}_x\text{Fe}_{2.5-x}\text{O}_4$ synthesized by sol–gel auto-combustion

Table 1 Structural and morphological parameters of $\text{Li}_{0.5}\text{Al}_x\text{Fe}_{2.5-x}\text{O}_4$ by sol–gel auto-combustion

Al^{3+} content (x)	Molar mass	Jump length (d_A) nm	Jump length (d_B) nm	Crystallite size (D) nm	Magnitude of micro-strains (ϵ)	Lattice constant (a), nm	Specific surface area $10^6 \text{ sm}^2/\text{g}$
0.2	201.27	0.2950	0.3612	10.3	0.0026	8.3426	0.534
0.4	195.49	0.2947	0.3610	9.6	0.0016	8.3366	0.330
0.6	189.72	0.2948	0.3610	13.6	0.0012	8.3376	0.394
0.8	183.95	0.2944	0.3606	14.2	0.0014	8.3274	0.523
1.0	178.17	0.2944	0.3606	23.6	0.0038	8.3271	0.242

**Fig. 2** X-ray diffraction spectra of $\text{Li}_{0.5}\text{Al}_x\text{Fe}_{2.5-x}\text{O}_4$ synthesized by ceramic method

were determined from the FWHM measurement as the Debye–Scherrer method of the most intense peak (311), as well as by the Williamson–Hall method, taking into account all well-separated peaks. Obtained crystallite sizes increase from 10.3 to 23.6 nm on increasing aluminum doping which is tabulated in Table 1. The lattice parameter decreases with increasing Al^{3+} content, as shown in Table 1. The lattice parameter value obtained for the synthesized samples is commensurate with the values typical of spinel ferrites (Kaykan et al. 2020). The decrease in the lattice parameter with the composition is explained on the basis of Vegard’s law (Poudel et al. 2019). The law gives a linear dependence of the lattice parameter on the ionic radius of embedded and removed ions. In this case, we replace the Fe^{3+} ion with Al^{3+} , because the ionic radius of Al^{3+} (0.067 nm) which is less than the ionic radius of Fe^{3+} (0.073 nm). Thus, the replacement of the Fe^{3+} ion by Al^{3+} leads to a decrease in the lattice parameter of the ferrite.

The X-ray spectra of $\text{Li}_{0.5}\text{Al}_x\text{Fe}_{2.5-x}\text{O}_4$ ($0 \leq x \leq 1$) samples synthesized by ceramic method are shown in Fig. 2. X-ray analysis revealed presence of impurity phases along with spinel phase, $\alpha\text{-Fe}_2\text{O}_3$ phase at $x=0.8$ and presence of $\sigma\text{-Al}_{2.667}\text{O}_4$ phase at $x=0.8$. The phase composition of composition $\alpha\text{-Fe}_2\text{O}_3$ phase and $\sigma\text{-Al}_{2.667}\text{O}_4$ phase are shown in Table 2.

Table 2 Phase composition of $\text{Li}_{0.5}\text{Al}_x\text{Fe}_{2.5-x}\text{O}_4$ ($0.0 \leq x \leq 1.0$) samples by ceramic method

Phase	Al^{3+} content (x) in $\text{Li}_{0.5}\text{Al}_x\text{Fe}_{2.5-x}\text{O}_4$				
	0.2	0.4	0.6	0.8	1.0
$\text{Li}_{0.5}\text{Al}_x\text{Fe}_{2.5-x}\text{O}_4$	100	74.45	93.17	94.54	92.08
$\alpha\text{-Fe}_2\text{O}_3$	0	21.55	6.83	5.06	0
$\sigma\text{-Al}_{2.667}\text{O}_4$	0	0	0	2.66	7.09

The distribution of cations on the sublattices of the system obtained by the solid-state reaction is shown in Fig. 3. Lithium and aluminum ions are in octaposition, and iron ions Fe^{3+} are distributed in both octa- and tetraposition. In addition, under conditions of prolonged exposure at high temperatures and relatively slow cooling, the so-called ordered phase of the spinel is formed. Cations of $\text{Li}^+(\text{Fe}^{3+}, \text{Al}^{3+})$ in the B-site are located in a ratio of 1:3 in the crystallographic direction (110), as also observed in the case of unsubstituted lithium iron spinel ($x=0$). That is, because of the phase transition “ordering—disordering” (Darul et al. 2005; Arillo et al. 2004) the spatial group $\text{Fd}3\text{m}$ decreases to $\text{P}4_132/\text{P}4_332$.

The change in X-ray density, sample density and porosity of the all samples using Archimedes’ principle are tabulated in Table 3. The table shows that the X-ray density decreases with increasing concentration of Al^{3+} ions. This can be explained by the fact that the density and atomic weight of Al atoms (2.702 and 26.98154 g/cm^3) are smaller than Fe atoms (7.86 and 55.847 g/cm^3), thus sample density shows the same dependence as the X-ray density. X-ray density is higher than the sample density indicates the pores structure in the samples, which is higher in samples synthesized by ceramic method due to sintering. Table 3 shows the dependence of the porosity of the samples on the composition also. The porosity of the samples increases with the composition for both systems; this is due to the lower density of Al^{3+} ions. The increase in porosity can also be explained based on the size of the crystallites. It can be noted that as the particle size decreases, the porosity increases in the range of 1.7–10.3% (El-Fadl et al. 2019).

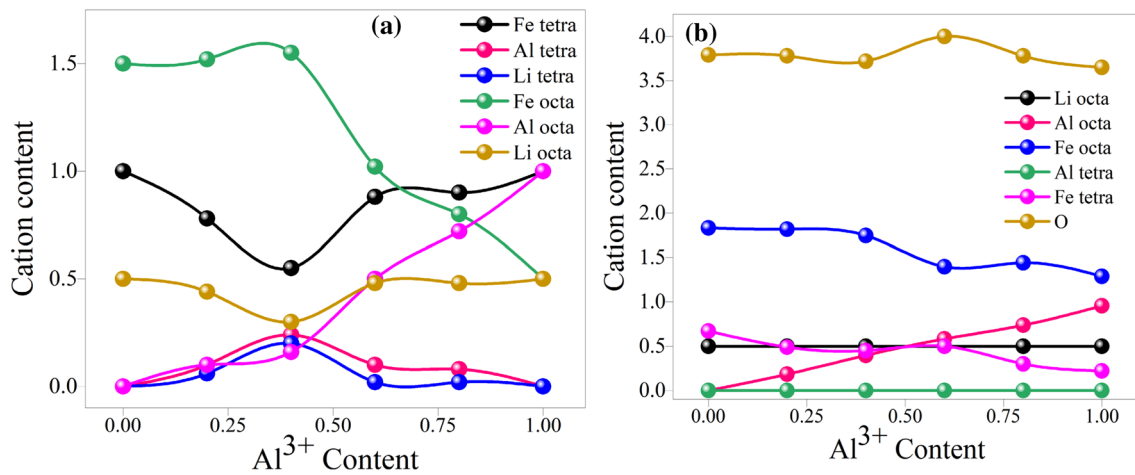


Fig. 3 Distribution of cations in sublattices vs. Al³⁺ ion content in Li_{0.5}Fe_{2.5-x}Al_xO₄ for **a** sol-gel auto-combustion method and **b** ceramic method

Table 3 X-ray density (D_x), sample density (D_s) and porosity (P) of Li_{0.5}Al_xFe_{2.5-x}O₄ samples

Al ³⁺ content (x)	D_x (g/cm ³) ± 0.01	D_s (g/cm ³) ± 0.01	P (%) ± 0.01	D_x (g/cm ³) ± 0.01	D_s (g/cm ³) ± 0.01	P (%) ± 0.01
	Synthesized by sol-gel auto-combustion			Synthesized by ceramic method		
0.2	4.15	3.52	14.01	5.06	3.57	29.41
0.4	4.09	3.46	15.10	5.27	3.22	38.84
0.6	4.04	3.38	15.32	4.99	3.22	35.48
0.8	3.97	3.21	17.31	4.98	3.59	27.88
1.0	3.92	3.20	19.15	4.71	3.40	27.95

Thus, comparing the structure and morphology of the samples synthesized by the traditional solid-phase reaction method and by sol-gel auto-combustion method, it is seen that the samples obtained by chemical method have higher homogeneity of element distribution by volume, good repeatability, high crystallinity, small crystallite size and perfect. In terms of cost-effectiveness, the sol-gel auto-combustion method does not require high-temperature long-term heat treatment in the synthesis process in contrast to the solid-phase method, which makes it possible to obtain high-quality ferrites with good characteristics at low cost.

Electrical properties

Figure 4a, b shows the change of the real and imaginary part of the dielectric constant of nanosized ferrite samples of the composition Li_{0.5}Al_xFe_{2.5-x}O₄ (0.0 ≤ x ≤ 1.0) with a frequency of 0.01–10⁵ Hz at temperature 293 K. As can be seen from the figures, all compositions exhibit a dielectric dispersion, where both the real and imaginary parts of the dielectric constant decrease rapidly with increasing frequency in the low-frequency region and almost do not depend on the frequency in the high-frequency region. The reduction of the imaginary part of the dielectric constant is

clearly greater than the real part. The dielectric dispersion curve can be explained on the basis of Coops' theory (Patel et al. 2017), which is based on the Maxwell–Wagner model for a homogeneous double structure (Mondal et al. 2014). According to this model, the dielectric structure is considered as a composition of double layers. The first layer is to some extent a well-conducting material, which is separated by a second thin layer (grain boundary) with relatively low conductivity. Grain boundaries have a greater effect at low frequencies while ferrite grains have a greater effect at high frequencies. The existence of a predominant number of Fe³⁺ ions and a smaller number of Fe²⁺ ions make the ferrite material dipolar.

The figure shows that all parameters increase with increasing Al³⁺ to x = 0.6, and decrease with subsequent increase in aluminum content. This can be explained based on the fact that Li ferrite has an inverted spinel structure and the degree of inversion depends on the heat treatment temperature and the method of production. Al³⁺ ions have an advantage in the B-position, while magnetic Fe ions occupy both tetrahedral and octahedral positions, so that substitution at low concentrations contributes to both the accumulation of charge at the grain boundaries and, accordingly, to increased polarization losses. With increasing aluminum

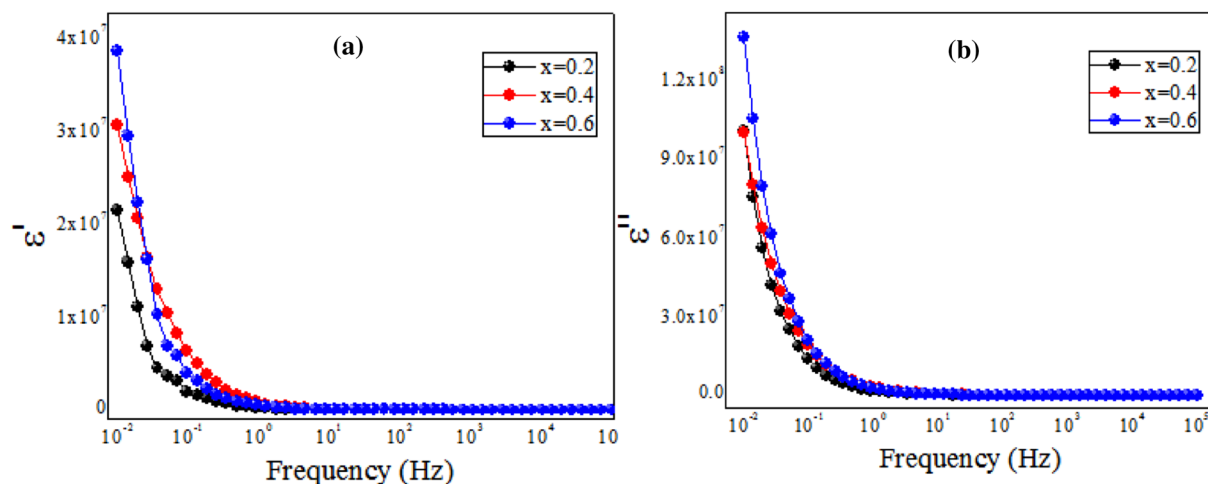


Fig. 4 **a** The real and **b** imaginary parts of the dielectric constant of samples obtained by the sol–gel auto-combustion

content ($x > 0.6$), due to the displacement of ions of variable valence from octa- to the tetra-sublattices, the accumulation of charge at the grain boundaries will decrease, and, accordingly, lead to a decrease in polarization.

However, in the case of fine particles, the grain–grain boundary makes a larger partial contribution compared to the bulk material, which makes the phenomenon more complex. Thus, in nanomaterials, additional conditions are created for obtaining high values of the dielectric constant due to significant surface polarization due to the large surface area of individual grains. In the low-frequency region, surface polarization plays a dominant role compared to electronic or ionic polarizations and determines the dielectric properties of the ferrite material (Aravind et al. 2014). In our measurements, ϵ' is of a very large order, 10^5 in pure and Al-substituted nanocrystalline $\text{Li}_{0.5}\text{Fe}_{2.5}\text{O}_4$ ferrites. A decrease in the value of the dielectric constant with increasing frequency is a normal dependence observed in most ferromagnetic materials. Polarization in ferrites occurs by a mechanism similar to conduction processes. Due to the electronic exchange between Fe^{2+} and Fe^{3+} , there is a local shift of electrons in the direction of the applied field and these electrons determine the polarization. The observed decrease in dielectric constant with increasing frequency is an attribute of the fact that the spatial charge carriers in the dielectric have a limited time for orientation in the direction of the external applied field. If the frequency of the alternating field increases, the moment is reached when the spatial charge carriers do not have time to turn in the direction of the field (Jha et al. 2019); as a result, the dielectric constant of the material decreases. When the field frequency is constantly increasing, at some stage the spatial charge carriers will only begin their reorientation, when the direction of the field has already changed and thus will not virtually contribute to the polarization and hence to the dielectric constant

of the material. High values of the dielectric constant at low frequencies are due to the presence in the samples of ions such as Fe^{2+} , oxygen vacancies, and defects at the grain boundaries, while the decrease in the dielectric constant with frequency is due to the fact that none of these contributions to the polarization of samples from changing the frequency of the applied field at high and ultrahigh frequencies (Gul et al. 2020).

Figure 5 shows the change in dielectric loss as a function of frequency from 0.01 to 10^5 Hz at room temperature (293 K). Dielectric losses give energy losses of the applied field in the sample. This is caused by the resonance of the domain walls. It was found that at high frequencies the losses are small because the motion of the domain walls is slowed down and the magnetization is caused by the change of rotation. There is a strong correlation between the conduction

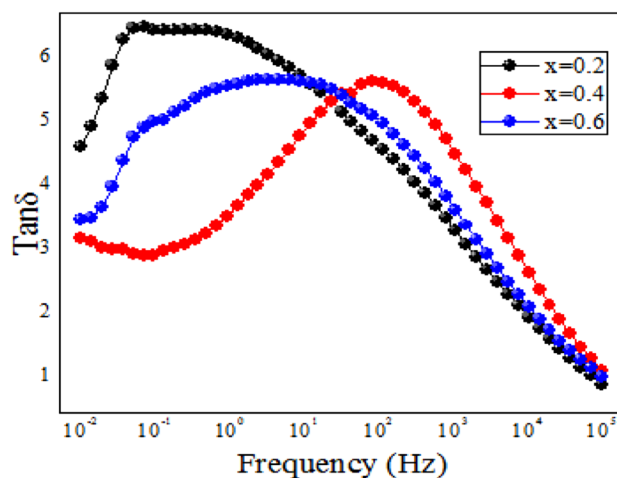


Fig. 5 The loss tangent of samples obtained by the sol–gel auto-combustion

mechanism and dielectric behavior in ferrites (Sartaj Aziz et al. 2019). From Fig. 5, it is seen that the dielectric losses have a peak for all compositions and there is a slight shift in the position of the maximum. It can also be noted that the peak height decreases with increasing Al concentration (Fig. 6).

The relation (1) determines conditions for the existence of a maximum of dielectric losses in the dielectric:

$$\omega\tau = 1, \quad (1)$$

where $\omega = 2\pi f_{\max}$ and τ is the relaxation time. From this relation, we can relate the relaxation time τ to the probability of a jump per unit time p as follows:

$$\tau = \frac{1}{2p}, \quad (2)$$

$$\text{or } f_{\max} \propto p. \quad (3)$$

Thus, these relations show that the maximum is observed when the jump frequency of electrons between Fe^{2+} and Fe^{3+} becomes approximately equal to the frequency of the applied field. Thus, the shift of the maximum towards lower frequencies with increasing Al concentration indicates that the probability of a jump decreases with increasing Al concentration. This decrease in the jump probability is an attribute of the decrease in the number of Fe^{3+} ions at the B-positions, which are responsible for the polarization in ferrites. The decrease in the peak height with increasing substitution of Al^{3+} ions is an attribute of the increase in the resistance of the samples due to the decrease in the pairs of $\text{Fe}^{3+}/\text{Fe}^{2+}$ ions responsible for the conductivity process. In this case, samples with $x = 0.6$ show the highest dielectric losses, which indicates the presence of a significant number of $\text{Fe}^{3+}/\text{Fe}^{2+}$ ions in octahedral sites.

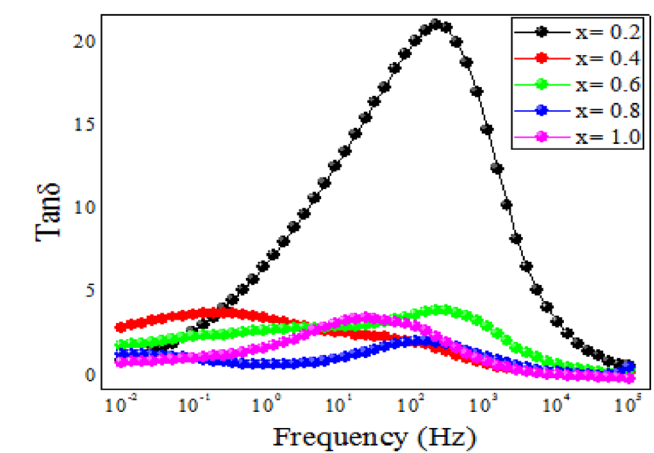
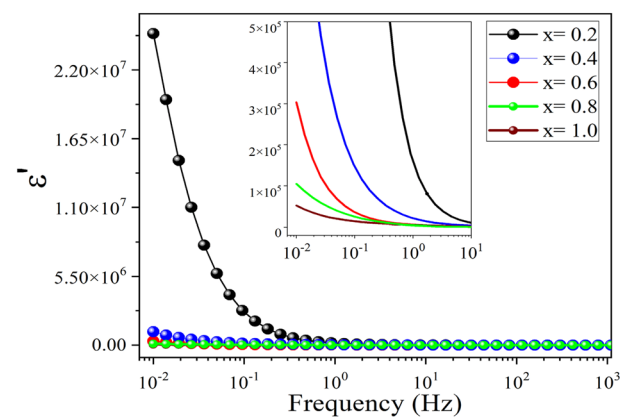


Fig. 7 The loss tangent of samples obtained by ceramic method

Figure 7 shows the change in the dielectric parameters ϵ' , ϵ'' , the loss tangent and the real and imaginary parts of the conductivity from the content of aluminum ions for the system obtained by the solid-phase method. Comparing the dependences of dielectric parameters on the aluminum ions concentration for systems obtained by different methods, as well as their nominal values, we can see that the samples obtained by the method of sol-gel auto-combustion have much better parameters compared to solid-phase samples. Obviously, this is due to the small size of the crystallites of auto-combustion samples and to the fact that of ceramic samples, in addition to the inclusions of the extraneous phase, has a rather inhomogeneous particle volume distribution. Particularly clear differences in the dielectric behavior of the two systems can be seen in the concentration dependences of the loss tangent. Thus, the maximum values of $\tan\delta$ for samples with sol-gel auto-combustion do not exceed the value of 6.38 for the considered frequencies, while the samples obtained by the ceramic method show the values of the

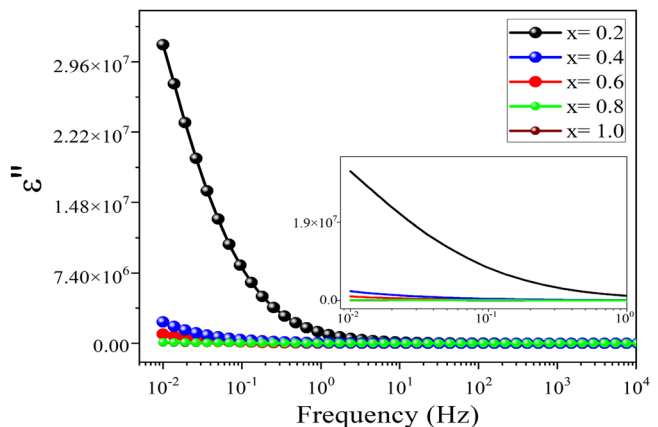


Fig. 6 a The real and b and imaginary parts of the dielectric constant of samples obtained by ceramic method, magnified parts show region 10^{-2} – 10^0 Hz

loss tangent of several hundred and even thousands. Thus, the method of sol–gel auto-combustion gives low-energy consumption ferrites with fairly good values of dielectric parameters.

Figures 8 and 9 show the real and imaginary parts of the electrical conductivity with a frequency from 0.01 to 10^5 Hz. The electrical conductivity in ferrites is mainly caused by the jump of an electron between ions of the same element present in more than one valence state, randomly distributed at crystallographic equivalent positions in the lattice. Ferrites form a cubic densely packed oxygen lattice in which cations occupy octahedral (B) and tetrahedral (A) sites. The distance between two metal ions in the (B) position is less than the distance between the two metal ions in the (B) and (A) positions, so a jump between (A) and (B) positions is much less likely than in the B–B jump. The jump between the A and A positions does not exist because they contain only Fe^{3+} ions, Fe^{2+} ions occupy only the B-position (Zaki et al. 2020). Charges can migrate under the influence of the

applied field, contributing to the electrical response of the system. It was found that the conductivity is an increasing function of frequency in the case of a hopping mechanism and decreasing in the case of band conductivity.

It can be noted that the value of conductivity gradually increases with increasing frequency of the applied field. The increase in σ_{AC} with frequency can be explained by the fact that the forcing force from the applied field of a certain frequency, which helps to transfer charge carriers between different localized states can also release the captured charges from different capture centers. Such charge carriers take part in conduction processes simultaneously with electrons exchanging metal ions in different valence states (Ni et al. 2020). The change n as a function of the Al content is shown in Fig. 10.

As is known from the literature, the value of n varies from 0 to 1. When n equal to zero, the electrical conductivity does not depend on frequency, i.e., there is DC conductivity, however, when $n \leq 1$, the conductivity depends

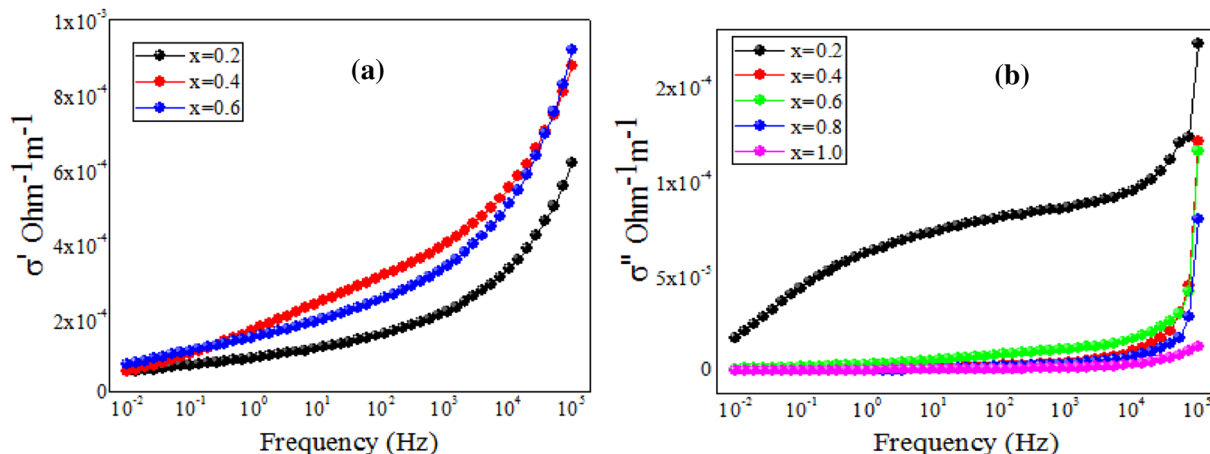


Fig. 8 The real (a) and imaginary (b) parts of conductivity of samples with sol–gel method

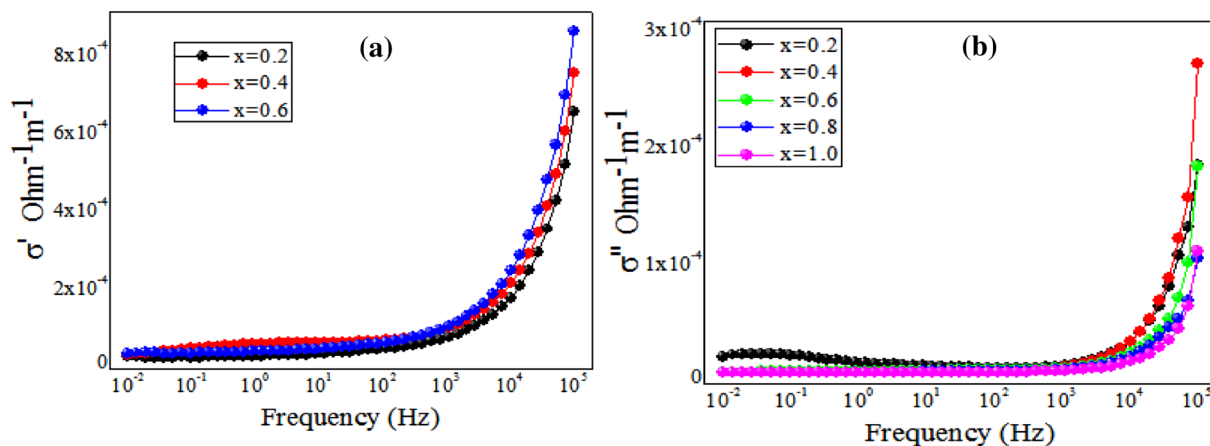


Fig. 9 The real (a) and imaginary (b) parts of conductivity of samples with ceramic method

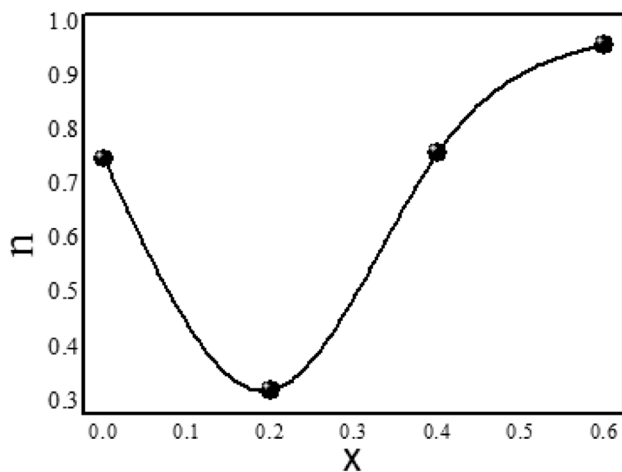


Fig. 10 Dependence of power factor n on composition

on frequency, or AC conductivity (Ni et al. 2020). In this work, the value of n varies around 0.293–0.995, which is a confirmation of the conductivity, which is the result of the jump.

From the figure, significant improvements in the conductivity of Al-substituted $\text{Li}_{0.5}\text{Al}_x\text{Fe}_{2.5-x}\text{O}_4$ are observed. Conductivity increases with increasing Al ion content to $x=0.1$, and then decreases with increasing Al concentration. For the sol–gel method of auto-combustion, this can be explained based on the fact that some of the iron ions of Fe^{3+} are usually reduced to the state of Fe^{2+} due to the annealing process at elevated temperatures (Maity et al. 2019). Fe^{2+} ions mainly occupy octahedral positions. In this case, the electronic conductivity occurs because of the jump of electrons between Fe^{2+} and Fe^{3+} in the octahedral positions. The increase in the AC conductivity of $x=0.4$ can be explained on the basis of the fact that the substitution of Al ions causes Fe^{3+} ions to migrate from tetrahedral to octahedral positions. An increase in the number of Fe^{2+} and Fe^{3+} ions in the octahedral positions, and thus, the substitution of Al can lead to an increase in the value of σ_{AC} . When the concentration of Al exceeds $x=0.1$, this leads to the migration of Fe^{3+} ions from the octahedral to the tetrahedral position, thus reducing the number of $\text{Fe}^{2+}/\text{Fe}^{3+}$ pairs in the B-positions, which are responsible for the conductivity in ferrites. For samples synthesized by the ceramic method, the strong increase in conductivity for $x=0.4$ is explained by the presence of the impurity phase ($\alpha\text{-Fe}_2\text{O}_3$).

Conclusion

Comparing the structure and morphology of the samples synthesized by the traditional solid-phase method and the sol–gel auto-combustion method, it is seen that the samples

obtained chemically have higher homogeneity of element distribution by volume, good repeatability, high crystallinity, small crystallite size and perfect stoichiometry. In terms of cost-effectiveness, the sol–gel auto-combustion method does not require high-temperature long-term heat treatment in the synthesis process in contrast to the solid-phase method, which makes it possible to obtain high-quality ferrites with good characteristics at low cost. Comparing the dependences of dielectric parameters on the concentration of aluminum ions for systems obtained by different methods, as well as their nominal values, we can see that the samples obtained by the method of sol–gel auto-combustion have much better parameters compared to solid-phase samples. Obviously, this is due in the first place to the small size of the crystallites of system A and also to the fact that system B, in addition to the inclusions of the extraneous phase, has a rather inhomogeneous particle volume distribution. The maximum values of $\tan\delta$ for samples with sol–gel auto-combustion do not exceed the value of 6.38 for the considered frequencies, while the samples obtained by the ceramic method show the values of the loss tangent of several hundred or even thousands. Thus, the method of sol–gel auto-combustion allows to obtain at low-energy consumption ferrites with fairly good values of dielectric parameters.

Acknowledgements The authors acknowledge faculty of Physical Engineering, Igor Sikorsky Kyiv Polytechnic Institute National Technical University of Ukraine for X-ray measurements, Faculty of Physics and Technology, Vasyl Stefanyk Precarpathian National University, Ukraine for Mössbauer measurements.

Compliance with ethical standards

Conflict of interest On behalf of all the authors, the corresponding author states that there is no conflict of interest.

References

- Sijo AK, Dutta DP, Roy M (2017) Dielectric properties of CoCrFeO_4 nano-powder prepared by solution self combustion synthesis. *Ceramics Int* 43(18):16915–16918. <https://doi.org/https://doi.org/10.1016/j.ceramint.2017.09.093>
- Aravind G, Ravinder D, Nathaniel V (2014) Structural and electrical properties of Li–Ni nanoferrites synthesised by citrate gel autocombustion method. *Phys Res Int* 2014:1–11. <https://doi.org/10.1155/2014/672739>
- Argentina GM, Baba PD (1974) Microwave Lithium ferrites: an overview. *IEEE Trans Microw Theory Tech* 22(6):652–658. <https://doi.org/10.1109/tmtt.1974.1128308>
- Arillo MA, López ML, Pico C, Veiga ML, Cuello G (2004) Order–disorder transition and magnetic ordering in lithium–titanium ferrites. *Phys B* 350(1–3):E301–E304. <https://doi.org/10.1016/j.physb.2004.03.075>
- Darul J, Nowicki W, Piszora P, Baecht C, Wolska E (2005) Synchrotron X-ray powder diffraction studies on the order–disorder phase transition in lithium ferrites. *J Alloy Compd* 401(1–2):60–63. <https://doi.org/10.1016/j.jallcom.2005.02.058>

- El-Fadl AA, Abd-Elrahman MI, Younis N, Afify N, Abu-Sehly AA, Hafiz MM (2019) Syntheses of new spinels Zn1-Fe Al₂O₄ nanocrystalline structure: Optical and magnetic characteristics. *J Alloy Compd* 795:114–119. <https://doi.org/10.1016/j.jallcom.2019.05.008>
- Gajula GR, Buddiga LR (2020) Structural, ferroelectric, dielectric, impedance and magnetic properties of Gd and Nb doped barium titanate-lithium ferrite solid solutions. *J Magn Magn Mater* 494:165822. <https://doi.org/10.1016/j.jmmm.2019.165822>
- Gul S, Yousuf MA, Anwar A, Warsi MF, Agboola PO, Shakir I, Shahid M (2020) Al-substituted zinc spinel ferrite nanoparticles: preparation and evaluation of structural, electrical, magnetic and photocatalytic properties. *Ceram Int* 46(9):14195–14205. <https://doi.org/10.1016/j.ceramint.2020.02.228>
- Jha VK, Sijo AK, Alam SN, Roy M (2019) Effect of Nd doping on structural, electrical, thermal and magnetic properties of multi-functional BiFeO₃ Ceramics. *J Supercond Novel Magn* 33(2):455–461. <https://doi.org/10.1007/s10948-019-05206-5>
- Kaykan LS, Mazurenko JS, Yaremiy IP, Bandura KV, Ostapovych NV (2019) Effect of nickel ions substitution on the structural and electrical properties of a nanosized lithium-iron ferrite obtained by the sol-gel auto-combustion method. *J Nano- and Electron Phys* 11(5):05041–1–05041–05047. [https://doi.org/10.21272/jnep.11\(5\).05041](https://doi.org/10.21272/jnep.11(5).05041)
- Kaykan LS, Mazurenko JS, Sijo AK, Makovysyn VI (2020) Structural properties of magnesium-substituted lithium ferrites. *Appl Nanosci* 10(8):2739–2747. <https://doi.org/10.1007/s13204-020-01259-4>
- Khan MZ, Gul IH, Baig MM, Khan AN (2020) Comprehensive study on structural, electrical, magnetic and photocatalytic degradation properties of Al³⁺ ions substituted nickel ferrites nanoparticles. *J Alloy Compd* 848:155795. <https://doi.org/10.1016/j.jallcom.2020.155795>
- Kopyayev AV, Mokljak VV, Gasyuk IM, Yaremiy IP, Kozub VV (2015) Structure ordering in Mg–Zn ferrite nanopowders obtained by the method of sol–gel autocombustion. *Solid State Phenom* 230:114–119. <https://doi.org/10.4028/www.scientific.net/ssp.230.114>
- Maity G, Maji P, Sain S, Das S, Kar T, Pradhan SK (2019) Microstructure, optical and electrical characterizations of nanocrystalline ZnAl₂O₄ spinel synthesized by mechanical alloying: Effect of sintering on microstructure and properties. *Physica E* 108:411–420. <https://doi.org/10.1016/j.physe.2018.10.024>
- Manikandan V, Singh M, Yadav BC, Denardin JC (2018) Fabrication of lithium substituted copper ferrite (Li-CuFe₂O₄) thin film as an efficient gas sensor at room temperature. *J Sci* 3(2):145–150. <https://doi.org/10.1016/j.jsamd.2018.03.008>
- Manikandan V, Kim J-H, Mirzaei A, Kim SS, Vigneselvan S, Singh M, Chandrasekaran J (2019) Effect of temperature on gas sensing properties of lithium (Li) substituted (NiFe₂O₄) nickel ferrite thin film. *J Mol Struct* 1177:485–490. <https://doi.org/10.1016/j.molstruc.2018.09.085>
- Mondal RA, Murty BS, Murthy VRK (2014) Maxwell-Wagner polarization in grain boundary segregated NiCuZn ferrite. *Curr Appl Phys* 14(12):1727–1733. <https://doi.org/10.1016/j.cap.2014.10.005>
- Ni Q, Sun L, Cao E, Hao W, Zhang Y, Ju L (2020) Structural, magnetic and dielectric properties of (Li¹⁺, Al³⁺) co-doped Ni_{0.5}Zn_{0.5}Fe₂O₄ ferrite ceramics prepared by the sol-gel auto-combustion method. *Current Applied Physics*, 20(9), 1019–1025. <https://doi.org/10.1016/j.cap.2020.06.012>
- Ostafijchuk BK, Bushkova VS, Moklyak VV, Initsky RV (2015) Synthesis and Magnetic Microstructure of Nanoparticles of Zinc-Substituted Magnesium Ferrites. *Ukrainian Journal of Physics*, 60(12), 1234–1242. <https://doi.org/10.15407/ujpe60.12.1234>
- Ostafijchuk BK, Gasyuk IM, Kaykan LS, Uhorchuk VV, Yakubovskiy PP, Tsap VA, Kaykan YS (2016) Temperature—Frequency Dependences of Dielectric Constants of Magnesium-Substituted Lithium Ferrite. *Metallofizika I Noveishie Tekhnologii*, 36(1):89–102. <https://doi.org/10.15407/mfint.36.01.0089> <https://doi.org/10.1021/cm011219v>
- Ostafijchuk BK, Kaykan LS, Kaykan JS, Deputat BY, Shevchuk OV (2017) Composition, microstructure, and electrical properties control of the powders synthesized by sol–gel auto-combustion method using citric acid as the fuel. *Nanoscale Research Letters*, 12(1). <https://doi.org/10.1186/s11671-017-1976-1>
- Patel CK, Solanki NP, Singh C, Jotania RB, Chauhan CC, Kulkarni SD, Shirsath SE (2017) Structural phases, magnetic properties and Maxwell–Wagner type relaxation of CoFe₂O₄/Sr₂Co₂Fe₁₂O₂₂ ferrite composites. *Materials Res Express* 4(7):076105. <https://doi.org/10.1088/2053-1591/aa7699>
- Patil RP, Hankare PP, Garadkar KM, Sasikala R (2012) Effect of sintering temperature on structural, magnetic properties of lithium chromium ferrite. *J Alloy Compd* 523:66–71. <https://doi.org/10.1016/j.jallcom.2012.01.025>
- Poudel TP, Rai BK, Yoon S, Guragain D, Neupane D, Mishra SR (2019) The effect of gadolinium substitution in inverse spinel nickel ferrite: Structural, Magnetic, and Mössbauer study. *J Alloy Compd* 802:609–619. <https://doi.org/10.1016/j.jallcom.2019.06.201>
- Sartaj Aziz H, Ali Khan R, Shah F, Ismail B, Nisar J, Mujtaba Shah S, Rahim A, Rahman Khan A (2019) Improved electrical, dielectric and magnetic properties of Al-Sm co-doped NiFe₂O₄ spinel ferrites nanoparticles. *Mater Sci Eng, B* 243:47–53. <https://doi.org/10.1016/j.mseb.2019.03.021>
- Saxena N, Kuanr BK, Zaidi ZH, Srivastava GP (1991) Effect of aluminium substitution on electric, magnetic, and microwave properties of LiTi ferrite. *Physica Status Solidi (a)* 127(1):231–242. <https://doi.org/10.1002/pssa.2211270126>
- Sijo AK, Dutta DP (2018) Size-dependent magnetic and structural properties of CoCrFeO₄ nano-powder prepared by solution self-combustion. *J Magn Magn Mater* 451:450–453. <https://doi.org/10.1016/j.jmmm.2017.11.092>
- Sijo AK, Jha VK, Dutta DP (2020) Structure and cation distribution in superparamagnetic NiCrFeO₄ nanoparticles using Mössbauer study. *J Magn Magn Mater* 497:166047. <https://doi.org/10.1016/j.jmmm.2019.166047>
- Soman VV, Nanoti VM, Kulkarni DK (2013) Dielectric and magnetic properties of Mg–Ti substituted barium hexaferrite. *Ceram Int* 39(5):5713–5723. <https://doi.org/10.1016/j.ceramint.2012.12.089>
- Zaki HM, AL-Heniti SH, Aljwiher MM (2020) Synthesis, structural, magnetic and dielectric studies of aluminum substituted cobalt-copper ferrite. *Physica B* 597:412382. <https://doi.org/10.1016/j.physb.2020.412382>